Effect of phase transformations on laser forming of Ti–6Al–4V alloy

Y. Fan,[a] P. Cheng, and Y. L. Yao
Department of Mechanical Engineering, Columbia University, New York, New York 10027

Z. Yang and K. Egland
Technical Center, Caterpillar Inc., Peoria, Illinois 61656

(Received 15 March 2005; accepted 6 May 2005; published online 7 July 2005)

In laser forming, phase transformations in the heat-affected zone take place under steep thermal cycles, and have a significant effect on the flow behavior of Ti–6Al–4V alloy and the laser-forming process. The flow-stress data of a material are generally provided as only dependent on strain, strain rate, and temperature, while phase transformations are determined by both temperature and temperature history. Therefore, effect of phase transformations on the flow behavior of materials in thermomechanical processing is not given necessary considerations. In the present work, both the $\alpha \rightarrow \beta$ transformation during heating and the decomposition of β phase, producing martensite α' or lamellae α dependent on cooling rate, are numerically investigated. The spatial distribution of volume fractions of phases is obtained by coupling thermal and phase transformation kinetic modeling. Consequently, the flow stress of Ti–6Al–4V alloy is calculated by the rule of mixtures based on the phase ratio and the flow stress of each single phase, which is also a function of temperature, strain, and strain rate. According to the obtained flow-stress data, the laser-forming process of Ti–6Al–4V alloy is modeled by finite element method, and the deformation is predicted. A series of carefully controlled experiments are conducted to validate the theoretically predicted results. © *2005 American Institute of Physics*. [DOI: 10.1063/1.1944202]

I. INTRODUCTION

Laser forming is a flexible thermal-forming process, during which laser beam causes local thermal expansion, and deformation is obtained by nonuniform release of thermal stresses during cooling. In the past two decades, great progresses have been made in understanding the laser-forming mechanisms[1,2] and investigating the effects of important process parameters on deformed shape and mechanical properties of the formed parts.[3–7] In particular, considerable research has been carried out on the computer modeling of laser forming. However, the application of numerical modeling is limited by lack of precise data of the temperature- and strain-rate-dependent flow stresses of materials. The flow-stress data were usually obtained directly from experiments or the constitutive equation based on limited experimental data. The experiment is cumbersome and time consuming, and flow-stress data must be obtained under steady temperatures. That is, the experimentally obtained flow-stress data are valid only under phase equilibria, and are not accurate under transient phase transformations like that in laser forming. With very fast heating and cooling, laser forming is significantly different from other hot-working processes. In laser-forming process, steep temperature gradients and thermal cycles lead to severe microstructural changes in the heat-affected zone (HAZ) within very short time. Therefore, it is necessary to consider the effects of phase transformations on laser forming. In this work, a methodology has been introduced to model flow behavior under transient phase transformations in laser forming, in which the contribution of each phase to flow stresses was calculated by the mixture rule based on its volume fraction. The temperature-, strain-, and strain-rate-dependent flow-stress data of every single phase can be obtained from experiments. The prerequisite to apply the methodology is that the kinetic details about the microstructural evolution are well known. With recent developments in computer simulation of phase transformations based on the fundamental kinetic and thermodynamic theories, it is possible to introduce those techniques to describe the particular laser-forming process.

Ti–6Al–4V alloy is a $(\alpha+\beta)$ two-phase alloy with around 6 wt % aluminum stabilizing the α phase and about 4 wt % vanadium stabilizing the β phase. At room temperature, the microstructure at equilibrium consists mainly of primary α phase (hcp) with some retained β phase (bcc). The physical and mechanical properties of Ti–6Al–4V alloys are known to be sensitive to their microstructure. The Ti-β phase having a diffusivity two orders of magnitude higher than that in the Ti-α phase, and the flow stress is strongly influenced by the ratio of the two phases present.

By combination of experiments and modeling, in this work we seek to quantitatively understand the kinetics of phase transformation during laser forming of Ti–6Al–4V alloy and their influence on flow behavior and deformation. In particular, the $\alpha \rightarrow \beta$ phase transformation during rapid heating and the decomposition of the β phase during rapid cooling were considered. During rapid heating, the kinetics of $\alpha \rightarrow \beta$ phase transformation have been extensively investigated by other researchers,[8–11] and the process can be modeled by the modified Johnson–Mehl–Avrami (JMA) equation for nonisothermal process. The decomposition of the β phase during cooling is much more complicated, and the product is martensitic α' or a secondary α phase with different mor-

[a]Electronic mail: yf2121@columbia.edu

TABLE I. Chemical composition of Ti–6Al–4V alloy in wt. %.

Al	V	Fe	C	N	O	H	Ti
6.24	3.98	0.40	0.01	0.05	0.20	0.015	Bal.

phology depending on cooling rates. Ahmed and Rack[9] investigated the phase transformations during cooling in Ti–6Al–4V alloy, and concluded that the martensitic transformation takes place with a cooling rate above 410 K/s. Slower cooling rates lead to diffusion-controlled nucleation and growth process of secondary lamellae α into the β grains. The diffusion controlled $\beta \rightarrow \alpha$ phase transformation during cooling can also be modeled by JMA equation.[12]

The objective of this work is therefore to investigate the phase transformations during laser forming of Ti–6Al–4V alloy and propose a method to consider their effects on the alloy flow behavior during the forming process. A thermal–microstructural–mechanical model was developed in the present work to quantitatively understand the complex laser-forming process with rapid heating and cooling. To validate the theoretically predicted results, a series of carefully controlled experiments are conducted.

II. MATERIAL AND EXPERIMENTS

A. Material

A commercial grade Ti–6Al–4V alloy is used in the present work and its chemical composition is shown in Table I. As-received plates of 0.8-mm thickness in the mill-annealed condition were used for testing. The starting microstructure is shown in Fig. 1. It consisted of equiaxed alpha with some amount of intergranular β. The initial volume fraction of β phase was measured by x-ray diffraction (XRD), and the XRD pattern is shown in Fig. 2. The contents of the initial α and β phases in the starting microstructure were estimated from the integrated peak areas of the α (101) and β (110) peaks. XRD also examined whether the alloy was induced texture by the prior thermomechanical treatment. Texture means that there is a pronounced orientation of certain crystallographic planes relative to the processing direction. From the XRD pattern shown in Fig. 2, there is not any highly favorable-oriented crystallographic plane, and therefore, the received Ti–6Al–4V alloy used in this study is thought to be texture-free.

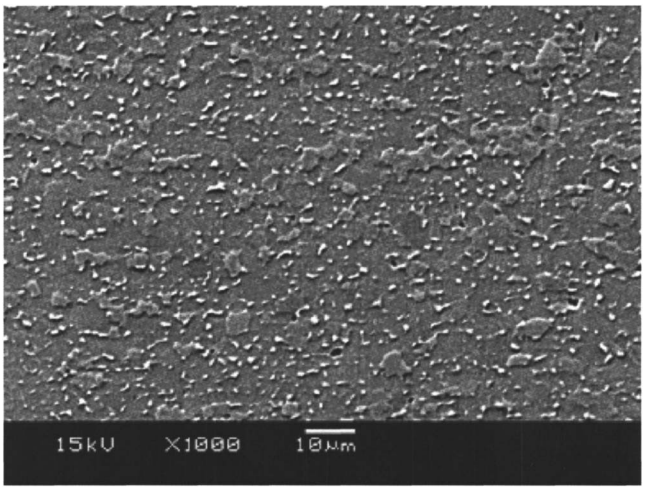

FIG. 1. The microstructure of the as-received Ti–6Al–4V alloy used in this study.

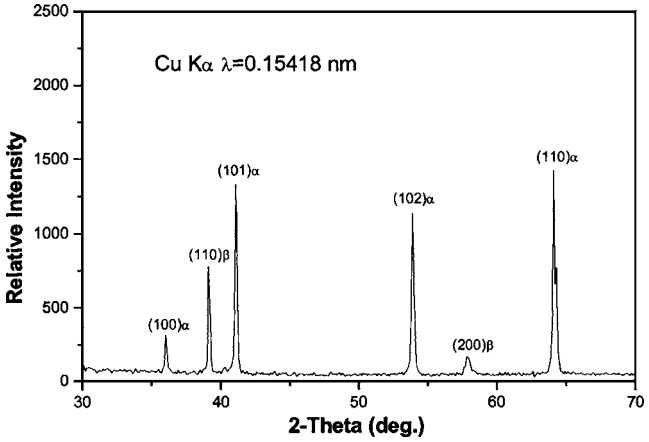

FIG. 2. Initial XRD pattern taken on the Ti–6Al–4V plate prior to laser forming.

B. Experiment

First of all, the starting microstructure of the Ti–6Al–4V alloy used in the present study was tested by XRD. The specimens for XRD, approximately 5×5 mm^2, were ground and polished on the surface to be examined.

Ti–6Al–4V alloy plates of $80 \times 80 \times 0.8$ mm^3 (shown in Fig. 3) were then laser scanned straight along the center line (X direction) under different conditions: 1000 W and 60 mm/s and 500 W and 30 mm/s, maintaining spot size of 6-mm diameter. To enhance laser absorption by the plates, a graphite coating was applied to the surface exposed to the laser. The laser system used was a PRC 1.5-kW CO_2 laser with TEM_{00} mode.

After scanning, the bending angles of the formed plates were measured by a coordinate-measuring machine (CMM). The plates were cross sectioned perpendicular to the scanning path, polished, and etched. The changes of macro- and microstructures in the HAZ were observed under scanning electron microscopy (SEM).

III. MODELS

A. Phase transformations

1. Heating

During heating, the phase transformation $\alpha \rightarrow \beta$ takes place when temperature is increased up to the starting point of the transformation, and then the β phase grows at the expense of the α phase, eventually reaching 100% β phase at the β transus temperature, approximately, 1273 K. The $\alpha \rightarrow \beta$ transformation in Ti–6Al–4V alloy involves the nucleation of the β phase from the α matrix and the growth of the β phase by diffusion. Therefore, the JMA equation is applicable to describe the $\alpha \rightarrow \beta$ transformation in Ti–6Al–4V alloy. This equation is expressed as

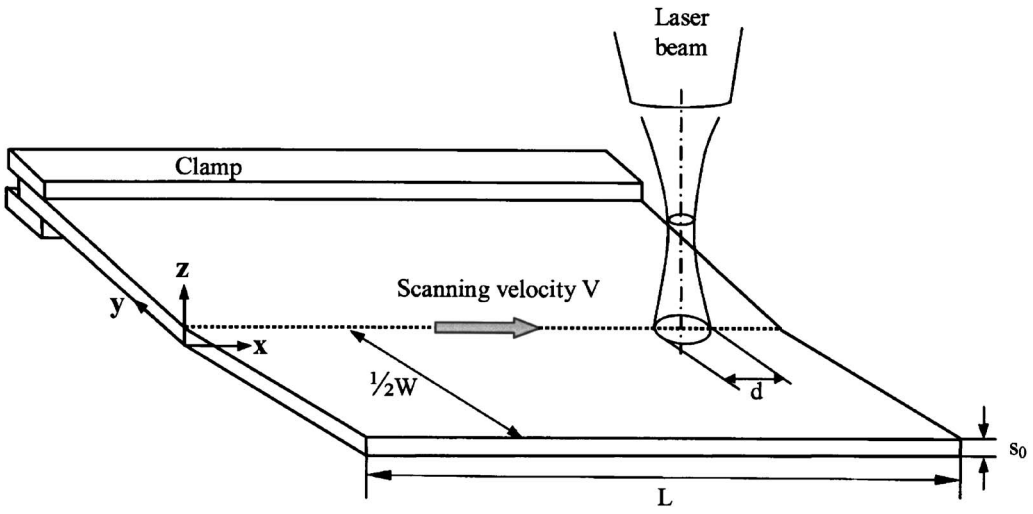

FIG. 3. Schematic of straight-line laser bending of Ti–6Al–4V sheet: s_0 is sheet thickness, W sheet width, L sheet length, and d laser spot diameter.

$$f_\alpha(t) = (1 - \exp[-(kt)^n]) f_\alpha^{\text{ini}} = \left(1 - \exp\left[-\left\{k \sum_{i=1} \Delta t_i\right\}^n\right]\right) f_\alpha^{\text{ini}}, \quad (1)$$

where $f_\alpha(t)$ is the amount of α phase after a time t, f_α^{ini} is the initial volume fraction of the α phase of the as received alloy which is measured by XRD, k is the reaction rate constant, and n the Avrami index.

2. Cooling

During cooling, the product of the β phase decomposition could be secondary α or martensitic α' depending on cooling rates. The critical cooling rate[9] is around 410 K/s. When the cooling rate is less than the critical cooling rate, the transformation is a diffusion-controlled nucleation and growth process of secondary lamellae α, and it is also valid to model the transformation by JMA theory. During cooling, the modified JMA equation could be expressed as

$$f_\alpha(t) = (1 - \exp[-(kt)^n])(f_\alpha^{\text{ini}} - f_\alpha^{\text{rem}}) = \left(1 - \exp\left[-\left\{k \sum_{i=1} \Delta t_i\right\}^n\right]\right)(f_\alpha^{\text{ini}} - f_\alpha^{\text{rem}}), \quad (2)$$

where f_α^{rem} is the volume fraction of the remained primary phase after heating. When the cooling rate is higher than the critical cooling rate, the β phase will transformed to martensitic α'. For the diffusionless transformations, the amount of martensite $f_{\alpha'}$ is calculated by an empirical formula,[13]

$$f_{\alpha'} = f'_\beta (1 - \chi \exp\{-(M_S - T)\}), \quad (3)$$

where f'_β is the volume fraction of the available β phase for martensitic transformation after heating, M_S is the martensitic transformation starting temperature, and χ is a material constant. It has been shown that around 10% β phase was retained independent of cooling rate as β phase was cooled to room temperature.[14] Therefore, the value of χ is made to be 0.003.

The values of the reaction-rate constant k and the Avrami index n during heating and cooling largely depend on the temperature and the mechanism of the transformation, and are not readily available. Malinov *et al.*[12] investigated the $\alpha \leftrightarrow \beta$ transformation kinetics of Ti–6Al–4V alloy and gave the values of k and n under different transformation mechanisms at different temperatures. Their result was applied in the present work (see Appendix A).

B. Flow stress

During laser forming, phase transformations take place in the HAZ and each present phase also undergoes work hardening and softening of dynamic recovery and recrystallization. Therefore, the strategy to model flow behavior is to calculate the flow stress of each single phase, which is also a function of temperature, strain, and strain rate, and then sum up the contribution of each phase by the rule of mixtures,

$$\sigma_{\text{total}} = \sum_{j=1}^{N} f_j \sigma_j, \quad (4)$$

where σ_{total} is the total flow stress, and f_j and σ_j are the volume fraction and the flow stress of the jth phase of the material, respectively. The information of phase ratio came from the modeling of phase transformation during heating and cooling, and the constitutive relations for the individual α and β phases can be fitted using a variety of flow-stress measurement. The constitutive relation for the single α phase of Ti–6Al–4V alloy with equiaxed microstructures was based on the measurements of Oikawa and Cui[15] and could be expressed by the following equation:[16]

$$\sigma_\alpha = \left[K_\alpha \exp\left(\frac{273\,000}{RT}\right)\dot{\varepsilon}\right]^{1/4.6}, \quad (5)$$

where R, T, and $\dot{\varepsilon}$ are the gas constant, temperature, and strain rate, respectively. The strength coefficient K_α represents the effect of the alloying elements, and the value is about 0.086 for the alloy in the present study. Similarly, the constitutive relation of the single beta phase was expressed as[16]

$$\sigma_\beta = \left[K_\beta \exp\left(\frac{160\,000}{RT}\right)\dot{\varepsilon} \right]^{1/4.2}, \tag{6}$$

in which the strength coefficient $K_\beta = 6.3$. Equations (5) and (6) were obtained from the data fitting using a variety of flow-stress measurements within the approximate temperature range of 1000–1300 K, and the flow stress almost remains constant when temperature is above 1300 K. For Ti–6Al–4V alloy, most of the deformation takes place as the temperature is above 1000 K with very rapid heating and cooling during laser forming. Therefore, it is assumed that Eqs. (5) and (6) are valid for the whole temperature range in the present study.

C. FEM thermal and mechanical models

A moving, continuous-wave (cw) laser irradiated the surface of a finite three-dimensional Ti–6Al–4V steel plate. The following assumptions are made in the formulation of the finite element model. The workpiece material is assumed to be isotropic, opaque, and with constant density. Material properties such as Young's modulus, yield stress, heat transfer properties, thermal conductivity, and specific heat are temperature dependent. Laser beam is vertical to the top surface of the workpiece. No melting is involved and no external forces are applied in the forming process. The heat flux of the moving laser beam follows Gaussian distribution,

$$q(x,y,t) = q_{\max} \exp\left[-\frac{3(x^2+y^2)}{4d^2} \right], \tag{7}$$

where d is the diameter of laser spot and $q_{\max}$ is the peak power density at the center of the laser spot.

The spatial and temporal temperature distributions $T(x,y,z,t)$ of a workpiece of dimensions $L \times W \times s_0$ (shown in Fig. 3) can be expressed by the three-dimensional heat conduction differential equation,

$$\rho c \frac{\partial T}{\partial t} = \nabla \cdot (K \Delta T), \tag{8}$$

where ρ, c, T, and K are the density, specific heat, temperature, and conductivity, respectively, x, y, and z are the Cartesian coordinates. The above governing equation is subject to the following boundary conditions: $y=0: T \to T_\infty$, $y=W: T \to T_\infty$; $Z=0: q(x,y,t)\cdot \hat{n} = -q(x,y,t)(k\nabla T)$. All of the six surfaces are subject to natural heat convection and radiation. $Q_{\text{conv}} = h(T-T_\infty)$ and $Q_{\text{rad}} = \varepsilon\sigma(T^4 - T_\infty^4)$, where h is the heat transfer coefficient, T_∞ is room temperature, and ε and σ are emissivity and Steffan–Boltzmann constant, respectively. The appropriate initial condition is $T(x,y,z,0) = T_\infty$.

The mechanical analysis during laser forming is based on the satisfaction of boundary conditions as well as compatibility and equilibrium conditions within the material volume in accordance with flow rules and yield criteria. The governing equation follows:

$$\frac{d}{dt}\int_V (\rho \vec{v}\cdot\vec{v}/2) + \rho U) dV = \int_S \vec{v}\cdot\vec{t} dS + \int_V \vec{f}\cdot\vec{v} dV, \tag{9}$$

where ρ is the density, $\vec{v}$ the speed field vector, U the internal energy per unit mass, $\vec{t}$ the surface traction vector, $\vec{f}$ the body force vector, V the volume, and S the corresponding boundary surface. If body force is neglected, the entire stress distribution of the material follows the equilibrium equation $\nabla \cdot \sigma = 0$. Because no external forces exert on the faces of the workpiece, the traction-free boundary condition is assumed, namely, $\sigma_{ij}\cdot\hat{n} = 0$. The total strain rate ε during laser forming can be decomposed into $(\varepsilon^e + \varepsilon^p + \varepsilon^{\text{th}} + \varepsilon^c)$, in which $\varepsilon^e, \varepsilon^p, \varepsilon^{\text{th}}$, and ε^c represent elastic strain rate, plastic strain rate, thermal strain rate, and creep strain rate. Due to the short thermal cycles in laser forming, the creep can be neglected. Therefore, the term $\dot{\varepsilon}_{ij}^c$ vanishes. The elastic strain can be expressed as

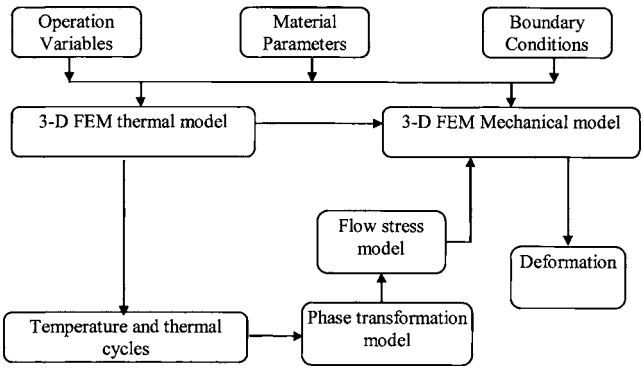

FIG. 4. Flow chart of the thermal–microstructural–mechanical modeling approach.

$$\sigma_{ij} = \lambda \varepsilon_{kk}^e \delta_{ij} + 2\mu \varepsilon_{ij}^e, \tag{10}$$

where σ_{ij} is the stress tensor, λ and μ are Lames's constants, and u is the displacement function. When the stress exceeds a critical magnitude, the stress-strain relation ceases to be linear, permanent or plastic deformations begin occur. In this case, Von Mises yielding criterion is used. According to the Von Mises criterion, yielding will occur when

$$\bar{\sigma} = \sqrt{\tfrac{3}{2}\left(\sigma_{ij} - \tfrac{1}{3}\delta_{ij}\sigma_{kk}\right)^2}, \tag{11}$$

where $\bar{\sigma}$ is the flow stress of the material and δ_{ij} is the Kronecker delta. For plastic deformation with the Von Mises criterion, the stress and strain relationship can be expressed as

$$d\varepsilon_{ij}^p = \frac{\partial g}{\partial \sigma_{ij}} d\lambda, \tag{12}$$

where λ is a function of stress that describes the yield criterion and g is the plastic potential function. The thermal strain ε^{th} is related to a temperature matrix $\mathbf{T}$ by a linear thermal expansion coefficient.

D. The thermal–microstructural–mechanical modeling

To systematically predict the laser-forming process based on the thermal–microstructural–mechanical modeling, the mathematical models described in the previous three sections need to be rationally arranged. Figure 4 shows the flow chart of the integration of these models.

The heating and deformation during laser forming are both symmetrical about the laser scanning path; therefore, only half of the plate $(80 \times 40 \times 0.8\text{mm}^3)$ is modeled in the

current research. The temperature field and thermal cycle are calculated from the three-dimensional (3D) thermal finite element model (FEM) modeling, and then the calculated temperature is input into the phase transformation model to get the volume fraction of each phase at a given time step. Because the phase transformation model requires very fine grids to assure enough accuracy, all phase transformations are only simulated on a cross section perpendicular to the scanning path of the plate. This is reasonable considering that all points along the scanning direction undergo similar thermal cycles and deformations when quasisteady state is reached. The flow stresses are calculated based on the phase volume fractions from phase transformation modeling. Finally, the temperature field and flow stresses are inputs into the mechanical model to calculate the thermal strain and predict the deformation. A commercial code, ABAQUS, was used to model the decoupled thermal and mechanical processes. In mechanical analysis, C3D20 element was applied, and the phase transformation and flow stress were calculated in the subroutine UHARD.

Two cases were run in the current research: $P=1000$ W and $V=60$ mm/s, and $P=500$ W and $V=30$ mm/s, where P represents power and V is the scanning velocity. In both cases, the laser beam spot size is 6 mm in diameter.

IV. RESULTS AND DISCUSSIONS

A. Initial phase ratio

The initial phase ratio of the α and β phases was measured by XRD. In the obtained XRD pattern shown in Fig. 2, the diffraction lines α (101) and β (110) were chosen to make quantitative analysis using the direct comparison method. According to the direct comparison method, we can obtain the following relationship:

$$\frac{I_\beta}{I_\alpha}=\frac{Af_\beta}{f_\alpha}=\frac{A(1-f_\alpha)}{f_\alpha}, \tag{13}$$

where f_α is the initial volume fraction of the α phase, f_β is the initial volume fraction of the β phase, and I_α and I_β are the measured integrated intensities corresponding to the α (101) and β (110) peaks, respectively. A was calculated to be about 1.67 (see Appendix B); therefore, the parameters f_α and f_β are calculated to be 0.75 and 0.25, respectively.

B. Macro- and microstructures from experiments

Figure 5(a) shows the SEM images of part of the laser-formed cross section perpendicular to the scanning path. A distinctly darkened region is observed. The darkened subregion is the HAZ, where phase transformation took place but no melting was involved. The size of the HAZ is measured to compare with the numerical results. Figure 5(b) shows the microstructure difference inside and outside the HAZ.

Figure 6 shows the microstructures at three different locations on the top surface in the HAZ under the conditions of 1000 W and 60 mm/s. In Fig. 6(a), martensite α' is observed at the center of the HAZ close to the scanning line. The α' phase is composed of long orthogonally oriented

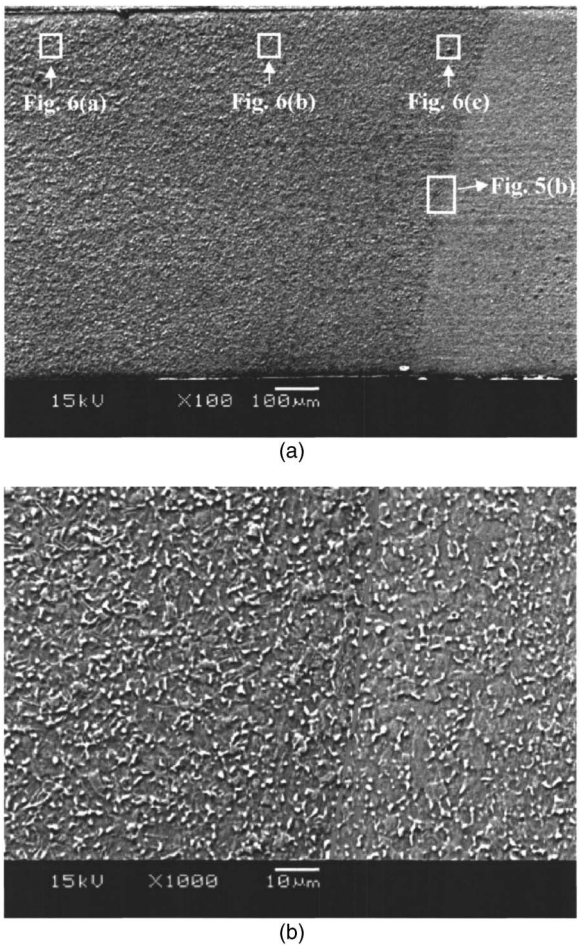

FIG. 5. SEM images of the cross section perpendicular to the scanning path. The HAZ and HAZ boundary were observed. Etched in Kroll's reagent, power=1000 W, and scanning speed=60 mm/s: (a) the HAZ and (b) microstructure difference across the HAZ boundary.

martensitic plate having an acicular morphology, and a substructure containing predominately dislocations and stacking faults with a few platelets containing twins. Clearly, α' is the dominant phase at the center of the HAZ, where the material experienced a very high cooling rate. Figure 6(b) shows that the main phase in the middle of the HAZ is the secondary Widmanstatten α, and this α morphology has a blocky appearance with a heavily dislocated internal substructure. A small amount of primary α is also observed from the SEM image. This primary α phase is the remained in transitional region after the $\alpha\rightarrow\beta$ transformation during heating. In the area close to the boundary of HAZ, the amount of the remained primary α increases and the block of the secondary α is smaller, which can be seen from Fig. 6(c). The case of 500 W and 30 mm/s shows an identical phase distribution within the HAZ.

Based on the experimental observation, the HAZ experienced significant phase transformations during the laser forming, as a result, the martensite α' was substantially formed due to high cooling rate at the center of the HAZ, and in the area further from the scanning line, the blocky secondary α was produced under a lower cooling rate. Some retained primary α was also found in the area close to the HAZ boundary. A small amount of retained β should also be pro-

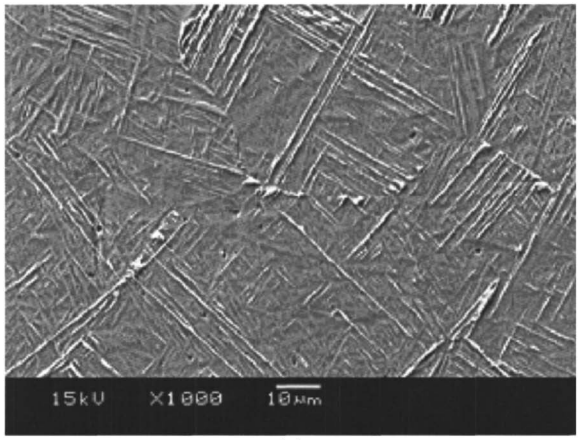

(a)

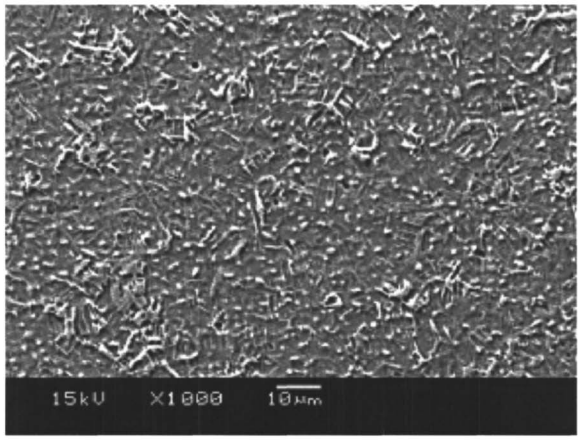

(b)

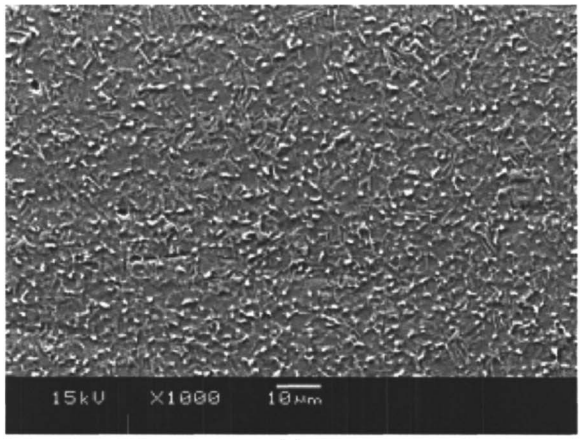

(c)

FIG. 6. Microstructure at different locations in the HAZ along Y direction after laser scanning, 1000 W and 60 mm/s: (a) close to the scanning path (heat source), (b) far from the scanning path, and (c) further from the scanning path, and close to the HAZ boundary.

duced in the HAZ, but it is generally in the form of thin film between martensite α' and secondary α plates, and cannot be observed from the SEM images.

C. Predictions by modeling

1. Thermal cycles

The calculated thermal cycles at different locations on the top surface of the scanned plate, obtained from FEM thermal model, are shown in Fig. 7. The figure shows that the

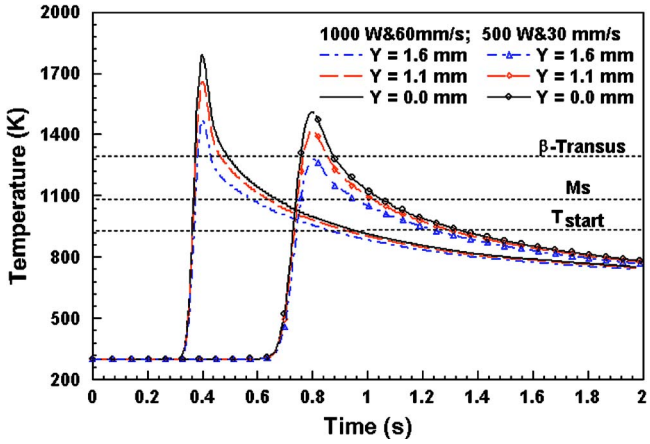

FIG. 7. (Color online) The calculated thermal cycles at different locations along y direction on the top of the HAZ as $X=20$ mm, from FEM thermal modeling of laser forming of Ti–6Al–4V alloy.

heating rate and the cooling rate were very large, and the magnitude of heating rate was up to 4×10^4 K/s. The very rapid heating and cooling would cause considerable superheating and undercooling during the laser forming. From Fig. 7, it is also found that the same line energy (P/V) caused different thermal results for the two cases, and that in the case of 1000 W and 60 mm/s a higher peak temperature was obtained. The reason is that the time for heat dissipation in the case of 1000 W and 60 mm/s was limited due to its faster scanning velocity. The heat loss was caused by convection, radiation, and conduction, but the heat loss caused by heat conduction was the main one. For the case of 1000 W and 60 mm/s, the main heat loss would be through the less time for heat conduction to allow the heat to flow away, so the heat loss was less.

2. Phase transformations

The phase transformation during heating is relatively simple because no melting is involved and only the $\alpha\rightarrow\beta$ transformation is considered. The process was predicted by the JMA equation. When the heating process has just finished and the cooling process is about to start, which is assumed to be when the peak temperature was reached, the calculated volume fractions of primary α and β are taken as the initial conditions for phase transformation during cooling.

Upon heating, the temperature where the dissolution of the primary α and the formation of the β phase start to take place was assumed to be T_{start} for this Ti–6Al–4V alloy. Therefore, between the temperature T_{start} and the β transus temperature, primary α and transformed β coexisted and formed a transitional region. 100% β phase was obtained when the temperature was above the β transus line (shown in Fig. 7). The values of T_{start} and the β transus are dependent on the chemical composition of the alloy and superheating, which causes the temperatures to shift up. From literature,[17,18] the value of T_{start} is around 913 ± 30 K and the β transus is about 1243 ± 50 K. In this model, the values of T_{start} and the β transus were assumed as 940 and 1273 K, respectively. In reality, the values of T_{start} and the β transus are varied with the rate due to superheating and undercool-

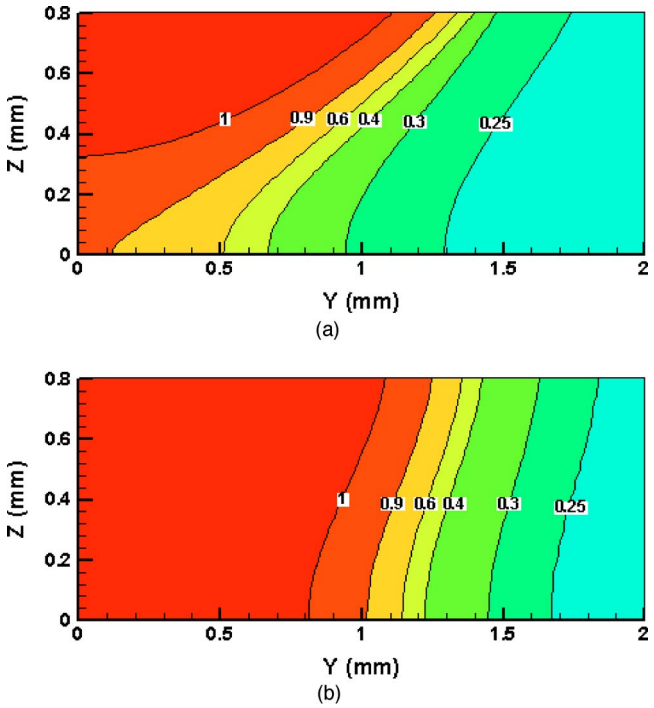

FIG. 8. (Color online) The distribution of volume fraction of β phase at the end of heating in the cross-section area perpendicular to scanning path only half of the area was modeled due to symmetry about Y: (a) $P=500$ W, $V=30$ mm/s and (b) $P=1000$ W, $V=60$ mm/s.

ing. However, in the phase transformation model T_{start} and the β transus were fixed during both heating and cooling. The effect of superheating and undercooling can be considered from the difference of the values of n and k during heating and cooling. The calculated β phase distributions at the end of the heating process (the points on the scanning line reached its peak temperature) for both cases are shown in Fig. 8. The contours in Fig. 8 show that the HAZ region in the case of 1000 W and 60 mm/s is larger than that in the case of 500 W and 30 mm/s because of a lower-energy loss. The comparison between the experimentally obtained and the calculated HAZ size is also given in Table II. The comparison shows that the numerical result is in good agreement with the experimentally obtained HAZ size.

To quantitatively predict the decomposition of the β phase in the HAZ during cooling, the cooling rates were first calculated from the 3D FEM thermal modeling. Whether the diffusion controlled $\beta \rightarrow \alpha$ transformation or the martensitic transformation would take place was then judged based on the cooling rates, and Eq. (2) and (3) was used based on the determined phase transformation mechanism. The calculated phase distributions after laser forming in the conditions of 1000 W and 60 mm/s are given in Fig. 9. From Fig. 9(a), the primary α in the transitional region was retained during the cooling process, and no changes happened to the volume fraction of primary α after heating. Figure 9(b) shows the volume fraction of martensitic α' formed in cooling. In the area close to heat source, the cooling rate is higher, and a substantial amount of martensite was formed. It must be emphasized, however, that for all cooling rates, a small amount of residual β phase remained after cooling. The amount of residual β phase was found to be 9 ± 2 wt % and independent of cooling rate.[12] In the current model, the residual β phase was assumed to be 10%. So in the area close to the heat source, the phases were comprised of (90% $\alpha'+10\%$ β). Even in the transitional region, some β phase transformed to martensite. The closer to the HAZ boundary, the lower the cooling rates. When cooling rates were under the critical rate, martensitic transformation stopped, and the diffusion-controlled $\beta \rightarrow \alpha$ transformation took place. That was why the volume fraction of martensite in the region close to the HAZ boundary was zero. Figure 9(c) shows the distribution of secondary α. The secondary α was only the product of the diffusion-controlled $\beta \rightarrow \alpha$ transformation, which took place under lower cooling rates. Figure 9(d) shows the distribution of β phase. Because the phase transformation mechanism in the region of martensitic transformation is different from the mechanism in the region of the diffusion-controlled $\beta \rightarrow \alpha$ transformation, the volume fraction of residual β is discontinuous across the two regions. In the region where martensitic transformation took place, the residual β phase is around 10%, and then gradually reduced with the $\beta \rightarrow \alpha$ transformation. Outside the HAZ, the β phase remained the initial 25% volume fraction. Similar numerical results were also obtained in the case of 500 W and 30 mm/s, and only the size of phases regions was different.

From the modeling, the final phase constitution after very steep thermal cycles during laser forming includes martensite α', remained primary α, secondary α, and a small amount of retained β in the HAZ. In fact, the secondary α can be divided into Widmanstatten and basket weave structure based on their morphology. The flow behavior of Ti–6Al–4V alloy is affected by the morphology and texture of the α phase, but because the deformation mainly took place when the temperature was above 1000 K and only lasted short time, their effects on the deformation were greatly limited under high temperature. Therefore, the effect of the morphology and texture of the α phase on flow stress were neglected.

3. Deformations

After the real time phase constitutive information is obtained by the phase transformation modeling, the flow behav-

TABLE II. Comparison of HAZ size between experimental and numerical results.

	HAZ top half-width (mm)		HAZ bottom half-width (mm)	
	Experimental	Numerical	Experimental	Numerical
500 W and 30 mm/s	1.73±0.05	1.76	1.32±0.03	1.29
1000 W and 60 mm/s	1.83±0.02	1.80	1.64±0.02	1.67

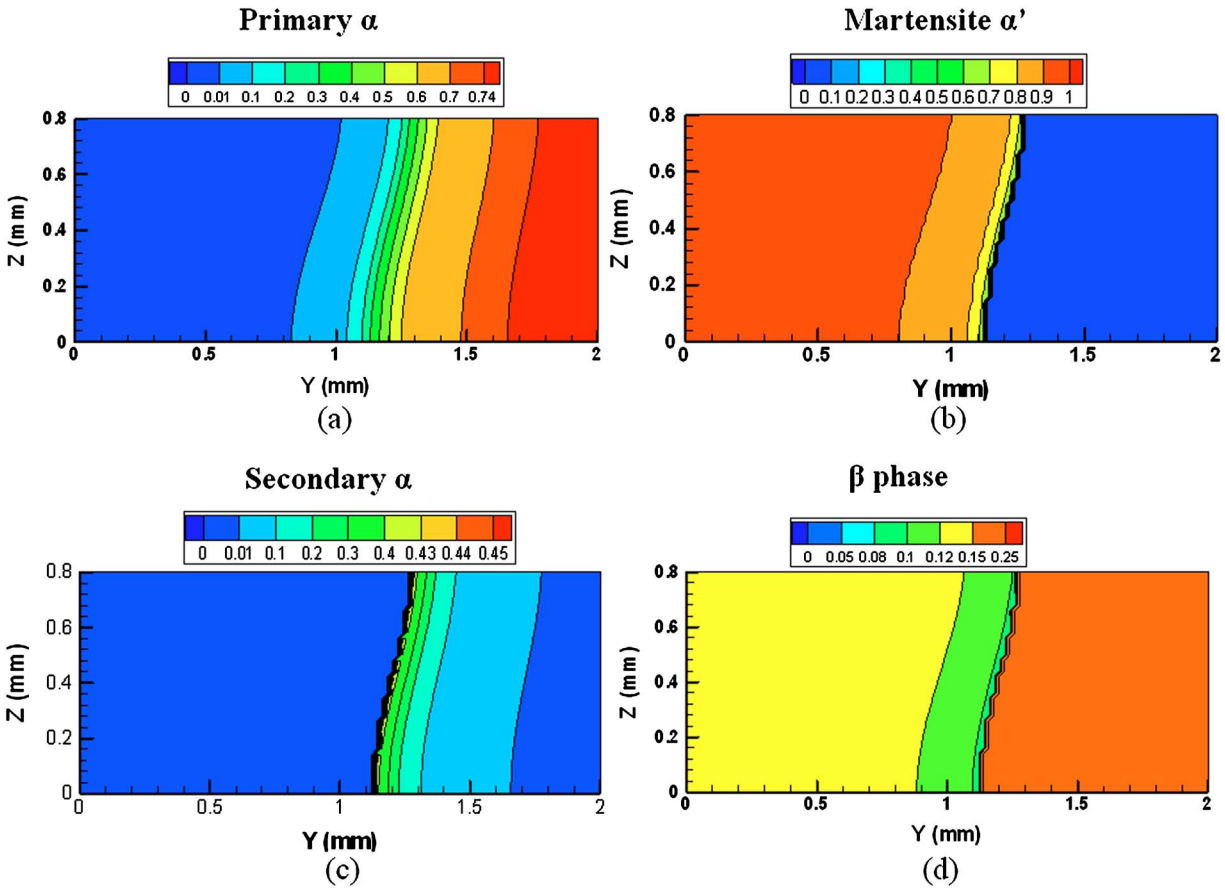

FIG. 9. (Color online) The calculated phase distribution after cooling, only half of the area was modeled due to symmetry about Y, $P=1000$ W and $V=60$ mm/s: (a) primary α, (b) martensite α', (c) secondary α, and (d) β phase.

ior can be calculated by the rule of mixtures using Eq. (4). Based on the calculated transient flow stress and the FEM mechanical modeling of laser forming, the bending angles of the plates can be predicted. The bending angles were also experimentally obtained. In the experiments of laser forming, it was found that the temperature gradient mechanism (TGM) was active for both cases despite the large laser beam diameter to sheet thickness ratio. This was attributed to the low thermal conductivity of the titanium alloy. Figure 10 shows that the experimental and the numerical results of the bending angles along the scanning path agree with each other very well when the effect of transient phase transformations on flow behavior was considered. It can be seen that, from the entering end of the scanning path ($X=0$ mm), the bending angle first drops a little and then increases to a greater angle at the exiting end. This phenomenon is called the edge effect and was already investigated in detail in an earlier research.[4] The drop of the bending angle after the laser enters the plate is caused by the stronger surrounding constraint in the middle of the plate. The bending edge curvature is dependent on the bending mechanism, constraint by the surrounding material and preheating. In the case of 1000 W and 60 mm/s, the scanning velocity was faster than that in the case of 500 W and 30 mm/s, and it was expected that the exiting end was preheated to a less extent. For Ti–6Al–4V alloy, however, the faster speed could not cause large difference on heat accumulation at the exiting end due to its very low thermal conductivity. In contrast, the higher input energy in the case of 1000 W and 60 mm/s caused easy buildup at the exiting end. Therefore, the increase of the bending angle at the exiting end was larger in the case of 1000 W and 60 mm/s than that of the 500 W and 30 mm/s case. Similarly, the bending edge curvature in the case of 1000 W and 60 mm/s was larger. To show the difference between including and not including transient phase transformations, nu-

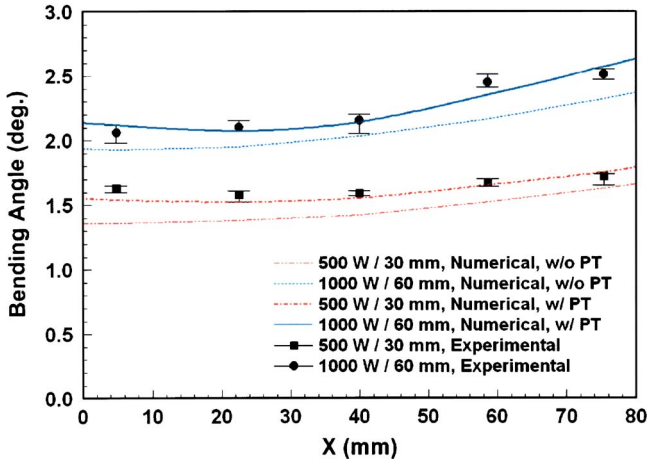

FIG. 10. (Color online) The comparison of numerically predicted bending angles with and without phase transformation (PT) consideration with experimentally obtained bending angles at various locations along scanning path ($Y=0$ mm).

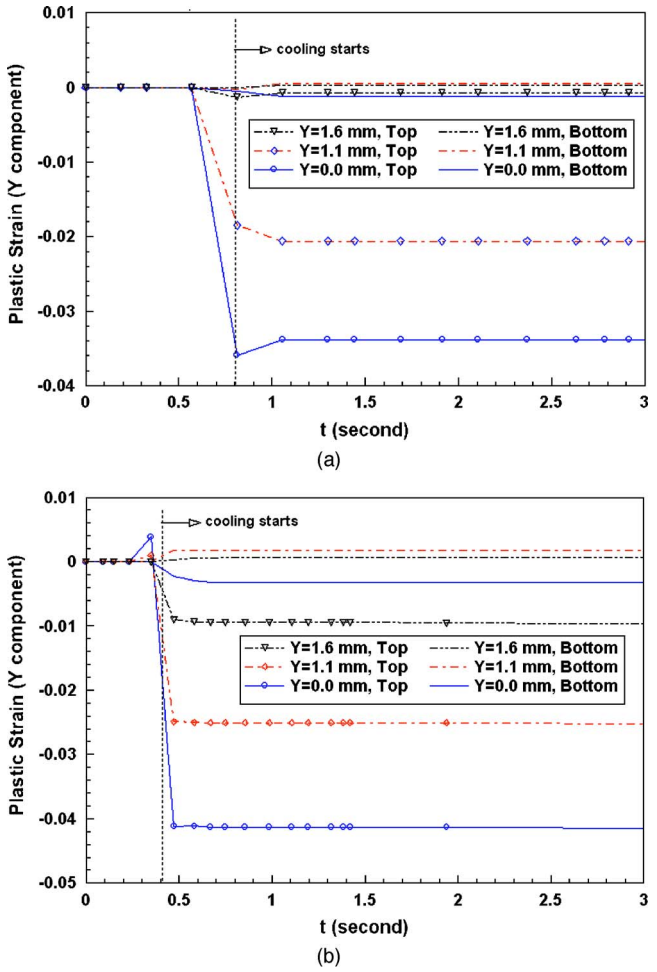

FIG. 11. (Color online) Y component of plastic strain at different locations along y direction on both the top and bottom as $X=20$ mm, from FEM mechanical modeling of laser forming of Ti–6Al–V alloy: (a) 500 W and 30 mm/s and (b) 1000 W and 60 mm/s. The time when cooling starts is defined as when the point at the scanning path ($X=20$ mm, $Y=0$ mm, and $Z=0.8$ mm) reaches the peak temperature.

merical modeling was also run by directly inputing flow-stress data, from literature,[19] as a tabular function of the equivalent strain, strain rate, and temperature, that is, the modeling did not consider the effect of transient phase transformations on flow stress. The numerical results are also shown in Fig. 10. Obviously, the numerical results with phase transformation consideration match the experimental results better.

Figure 11 shows the simulated history of the Y component of the plastic strain at different locations. As seen, the plastic strain is severely compressive at the top surface of the plate and slightly compressive of tensile on the bottom surface. These results are easily understood. During heating, the top of the plate tended to thermally expand, but the thermal expansion was restricted by the surrounding material, which led to the compressive plastic strain at the stage of cooling. The compressive plastic strain produced on the top made the plate bend towards the laser. It is the typical characteristics of temperature gradient mechanism.[1] In Fig. 11(a), the plastic strain on both top and bottom is also zero when $Y=1.6$ mm, which means that the width of plastic zone is only around 1.6 mm in the case of 500 W and 30 mm/s. Whereas, there is large compressive strain on the top even when $Y=1.6$ mm in Fig. 11(b). Meanwhile, Fig. 11 also shows that the plastic deformation took place within very short time, when the temperature was very high.

V. CONCLUSIONS

A thermal–microstructural–mechanical model has been developed for the laser forming process. The model considers the effect of phase transformations on the flow behavior of Ti–6Al–4V alloy. The phase transformations of Ti–6Al–4V alloy during laser forming were modeled based on the phase transformation kinetics, and the flow stress of Ti–6Al–4V alloy is predicted by the rule of mixtures. The predicted HAZ macrostructure, phase constitution, and bending angle are in good agreement with the experimental results. This indicates that the proposed modeling approach is able to predict the microstructure evolution and the deformation induced by laser-forming processes of dual-phase alloy.

ACKNOWLEDGMENTS

The authors acknowledge the financial support from NIST under Grant No. ATP-00005269. Helpful discussion with Dr. Judson Marte from General Electric Global Research Center is gratefully acknowledged.

APPENDIX A

The values of the reaction-rate constant k and the Avrami index n during heating and cooling given by Malinov *et al.*[12] are listed in Table III.

APPENDIX B

According to the direct comparison method, it was assumed that the relative integrated intensity of a given diffraction peak is given by[20]

$$R = F^2 p \frac{1}{v^2}\left(\frac{1+\cos^2 2\theta}{\sin^2\theta\cos\theta}\right)e^{-2M},$$

where F^2 is the structure factor and describes the effect of the crystal structure on the intensity of the diffracted beam, p is the multiplicity factor, which is the number families of planes independently contributing to the reflection, v is the volume of the unit cell, the term $[(1+\cos^2 2\theta)\sin^2\theta \times \cos\theta]$ is the Lorentz-polarization factor, and e^{-2M} is the

TABLE III. JMA kinetic parameters for Ti–6Al–4–V alloys used in the work (Ref. 12).

	n		k	
Temperature (K)	Heating	Cooling	Heating	Cooling
1023	1.40	1.35	0.028	0.033
1073	1.34	1.35	0.026	0.025
1123	1.38	1.35	0.022	0.024
1143	1.34	1.35	0.025	0.025
1175	1.21	1.1	0.046	0.068
1193	1.39	1.1	0.024	0.055
1223	1.41	1.1	0.017	0.045

TABLE IV. Calculated factors determining the intensities of the alpha (101) plane and the beta (110) plane.

	α (101)	β (110)
2θ	41.1	39.1
Lattice parameter, a (nm) (Ref. 21)	0.293	0.322
Lattice parameter, c (nm) (Ref. 21)	0.467	⋯
Volume of unit cell, v (nm^3)	0.03407	0.03246
Atomic scattering factor, f	15.30	15.43
Structure factor, F^2	701.537	952.710
Multiplicity factor, p	12	12
Lorentz-polarization factor	13.5889	15.184
Relative integrated intensity, R	9.855×10^7	1.6475×10^8
$A=R_\beta/R_\alpha$	1.672	

temperature factor, taking into consideration the effect of temperature on the intensity of the reflections. Data required for calculation of the temperature factor for alloys are not readily available and therefore it was here not accounted for. For the α (101) F is calculated from $3f^2\cos(5\pi/6)$ and for β (110) from $4f^2$, where f is the atomic scattering factor. The calculation of those factors determining the intensities of the alpha (101) plane and the beta (110) plane is shown in Table IV.

[1]F. Vollertsen, Mechanism and Models for Laser Forming, in Proceedings of LANE '94, 1994 (unpublished), Vol. 1, Sec. B, pp. 345–360.
[2]S. Holzer, H. Arnet, and M. Geiger, Extending Laser Bending for the Generation of Convex Shapes, in Proceedings of LANE '94, 1994 (unpublished), Vol. 1, Sec. B, pp. 379–386.
[3]W. Li and Y. L. Yao, ASME J. Manuf. Sci. Eng. **122**, 445 (2000).
[4]J. Bao and Y. L. Yao, Study of Edge Effects in Laser Bending, in Proceeding ASME IMECE 1999, 1999 (unpublished), MED-10, pp. 941–948.
[5]W. Li and Y. L. Yao, ASME J. Manuf. Sci. Eng. **123**, 674 (2001).
[6]J. Cheng and Y. L. Yao, J. Manuf. Process. **3**, 60 (2001).
[7]J. Cheng and Y. L. Yao, ASME J. Manuf. Sci. Eng. **124**, 379 (2002).
[8]J. W. Elmer, T. A. Palmer, S. S. Babu, W. Zhang, and T. DebRoy, J. Appl. Phys. **95**, 8327 (2004).
[9]T. Ahmed and H. J. Rack, Mater. Sci. Eng., A **243**, 206 (1998).
[10]W. Sha and Z. Guo, J. Alloys Compd. **290**, L2 (1999).
[11]J. W. Elmer, T. A. Palmer, and J. Wong, J. Appl. Phys. **93**, 1941 (2003).
[12]S. Malinov, P. Markovsky, W. Sha, and Z. Guo, J. Alloys Compd. **314**, 181 (2001).
[13]R. Trivedi, Acta Metall. **18**, 287 (1970).
[14]S. Malinov, Z. Guo, W. Sha, and A. Wilson, Metall. Mater. Trans. A **32A**, 879 (2001).
[15]H. Oikawa and M. Cui, in *High Temperature Deformation of Alpha-Titanium*, International Series on the Strength and Fracture (Pergamon Press, New York, 1986), Vol. 1, pp. 601–606.
[16]S. L. Semiatin, F. Montheillet, G. Shen, and J. J. Jonas, Metall. Mater. Trans. A **33A**, 2719 (2002).
[17]R. Pederson, O. Babushikin, F. Skystedt, and R. Warren, Mater. Sci. Technol. **19**, 1533 (2003).
[18]Y. Ro, H. Onodera, K. Ohno, T. Yamagata, I. Tomizuka, and M. Yamazaki, Trans. Iron Steel Inst. Jpn. **26**, 322 (1986).
[19]T. Seshacharyulu, S. C. Medeiros, W. G. Frazier, and Y. V. R. K. Pradad, Mater. Sci. Eng., A **284**, 184 (2000).
[20]B. D. Cullity, *Elements of X-Ray Diffraction* (Addison-Wesley, Reading, MA, 1978), p. 411.
[21]S. Malinov, W. Sha, Z. Guo, C. C. Tang, and E. A. Long, Mater. Charact. **48**, 279 (2002).